An imaging measurement system of electron beam spot based on CMOS sensor and error correction

LINGCHAO BAI[1,2], WEI HE[1,*], BOHUA YIN[2,3,*]
[1] *School of Instrument Science and Optoelectronics Engineering，Beijing Information Science and Technology University, Beijing 100192, China*
[2]*Research Department of Micro-nano Fabrication Technology and Intelligent Electronic Devices, Institute of Electrical Engineering, Chinese Academy of Sciences, Beijing 100190, China*
[3]*School of Engineering Sciences, University of Chinese Academy of Sciences, Beijing 100049, China*

The Scanning Electron Microscope (SEM) is essential for its exceptional resolution, especially in medical imaging, semiconductor technology, and nanomaterial characterization. This paper presents an optical imaging system that measures the SEM electron beam spot size using a magnification lens and a Complementary Metal Oxide Semiconductor (CMOS) sensor. The system acquires image data of a steel ruler and analyzes the correlation between unit length and pixel dimensions, the uncertainty of system is studied also. By analyzing the experimental data, a correction curve for the imaging system can be derived, and the corrected error is kept within ±0.043 μm.

(Received August 24, 2024; accepted February 3, 2025)

Keywords: Imaging system, Beam spot measurement, Error analysis, Error correction

1. Introduction

The advancement of technology and the evolution of advanced manufacturing industries resulted in a notable increase in the complexity of manufactured parts, accompanied by a corresponding intensification of precision requirements. Precision positioning and measurement techniques have garnered significant attention and have witnessed an increasing adoption across critical applications, including wafer defect inspection, small-scale robotics, and Computer Numerical Control (CNC) precision machining [1-3], among others. Traditional inspecting techniques rely on either manual labor or inspection devices. Although manual inspection is a relatively slow process, optical microscopes offer enhanced precision, reaching the micron level. However, they still have limited capability in meeting the demands of nanometer-level precision. In the field of microscopic imaging technology, several types of electron microscopy are extensively used in the biomedical and semiconductor industries, owing to their advantages of high precision, resolution, and depth of field [4-6]. As a critical inspection instrument, the SEM is capable of observing object surfaces at both micron and nanometer levels, including the microscopic structures of material surfaces, cellular structures, and biomolecules, with magnification ranging from tens to several million times.

SEM employs an electron beam to scan the surface of a material, converting the signals generated by the interaction between electrons and the material into images. This process enables the acquisition of high-resolution image information about the sample surface. The size of the electron beam spot has a direct impact on the resolution of the resulting image. Even minor discrepancies at the nanometer level can lead to significant error. Consequently, the accurate measurement of the beam spot's shape and size parameters is a significant area of research interest. The knife-edge method and the point scanning method are two techniques for measuring size characteristic of light beams or other charged particle beams, which have great importance in detecting electron source performance and alignment [7-10]. The knife-edge method entails intercepting the electron or laser beam with a sharp edge (such as a knife blade) and analyzing the resulting changes in the electron signal to study the dimensions of the beam spot [11,12]. This method makes use of the edge effect of the sharp edge, thereby enabling the accurate measurement of the beam spot. The point scanning method entails

scanning the electron beam spot point-by-point using an electron detector (such as a Faraday cup) and recording the distribution of the detected signal intensity, which provides a more precise measurement of the beam spot size. While these methods are capable of accurately measuring the size of an electron beam spot, they demand sophisticated and costly instrumentation, as well as a more extended measurement period. Thus, it is important to develop an affordable, easy-to-operate, and rapid measurement method to measure the size of electron beam spot. The measurement method entails the collection of target image data using high-quality image acquisition devices (primarily CCD or CMOS sensors) and subsequently analyzing the image data to obtain target information. This method is widely utilized in various industrial fields and production enterprises. K. Purvis et al. utilized the knife-edge method and CMOS sensors to quantify characteristics of laser beams, such as quality factors, ellipticity, and diameter [13]. Y. Tan et al. designed a low-cost beam profile prototype, utilizing the knife-edge method to measure the Full Width Half Maximum (FWHM) of a range of laser diodes [14]. J. Z. Jelic et al. reported an application of the knife-edge technique to measure lateral and axial resolution assessment of nonlinear laser scanning microscopy [15]. B.S. Rawat et al. investigated ion current using a Faraday cup array to measure the radial distribution of ion current density [16]. Previous studies have achieved accurate measurements of electron beam spots, although the major challenge in electron beam spot imaging is cost and image speed. The size of the electron beam spot is generally small, at the micron or nanometer scale. Even small errors can significantly affect its measurement, such as the calibration of errors in phosphor screen photoelectric conversion and camera systems. In study process, these subtle errors must be considered and relevant calibration must be performed to accurately measure the size of the light spot or electron beam spot. Thus, it is still important to investigate rapid imaging methods and error calibration for big beam spot precision measurements.

Here, an optical image measurement system is reported and the system combines an optical magnification lens and a CMOS sensor. The fundamental principles and root causes of image error are investigated. The imaging techniques employed and the subsequent data processing are discussed, which enables error analysis and measurement correction for the imaging system.

2. Principles and experimental

The optical microscope imaging system consists of primary components, including optical magnification lenses and a CMOS sensor. The optical lenses determine the magnification and numerical aperture (NA) of the overall imaging system, while influencing the working distance of the system. The CMOS sensor commonly used in digital imaging devices, is an integrated circuit that uses complementary metal oxide semiconductor (CMOS) technology, which is applied in the manufacture process of photosensitive elements. This sensor determines the pixel size and resolution of the image. The quality of the light source has a significant impact on image quality and resolution. In this system, the light source is a constant white LED light source that remains stable during operation. The imaging principle of CMOS sensors is based on photoelectric conversion and digital signal processing. The light ray passes through a lens and focuses on the photosensitive area, where the photodiode of each pixel generates a current proportional to the intensity of the light received. These currents are then amplified by an amplifier and converted into voltages, which are converted into digital signals by an analog-to-digital converter. Finally, these signals are transmitted to an image processing chip for further processing, including noise reduction, color interpolation, and white balance adjustment, to generate high-quality images. The overall experimental system is shown in Fig. 1. In the SEM system, the electron beam passes through condenser lens, the magnetic lens, objective lens, and other components before ultimately reaching the surface of the sample. The inner structure of the magnetic lens is generally composed of a solenoid or a multi-pole magnet structure, and its function is to focus and adjust the electron beam passing through the magnetic lens, the work process of SEM is shown in Fig. 1(a). The interaction between the electron beam and the sample is depicted in Fig. 1(b), this interaction results in the emission of secondary electron, backscattered electron, auger electron and X-ray. The imaging system is illustrated in Fig. 1(c) and Fig. 1(d).

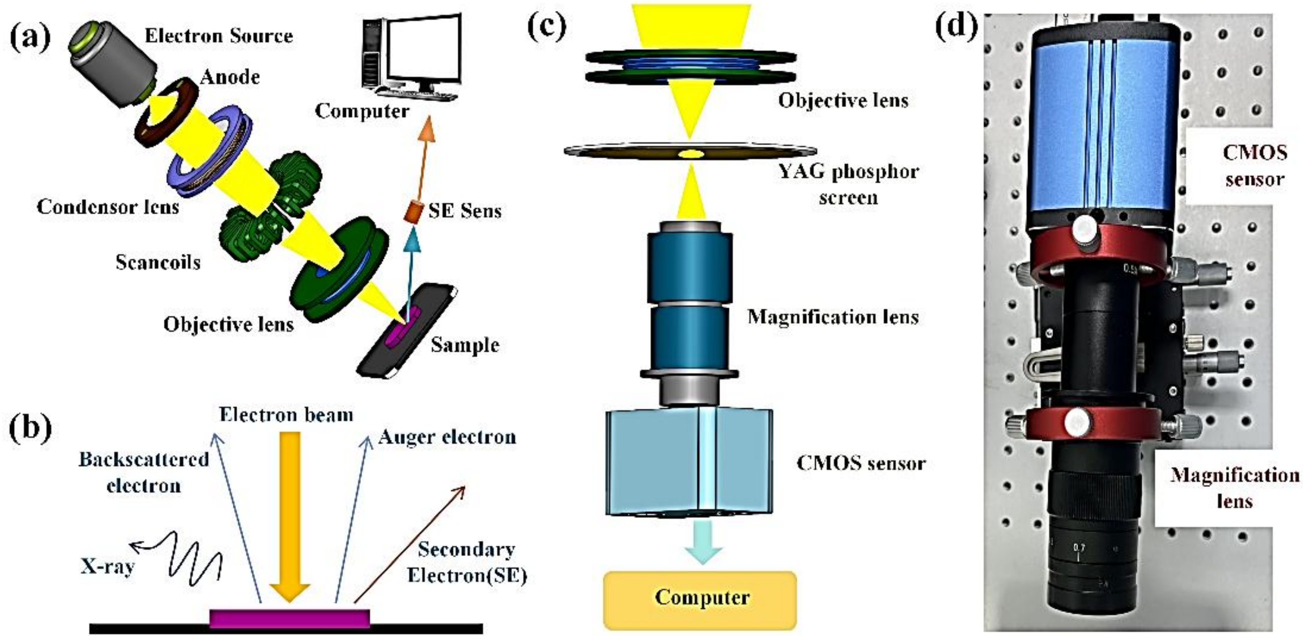

Fig. 1. Test system diagram (a) Scanning electron microscopy (SEM) (b) Interaction of electrons with the sample (c) SEM beam spot testing (d) Imaging system camera (colour online)

In this paper, the error correction relationship of the microscopic imaging system was studied by imaging the scale of a steel ruler and analyzing the sources of error within the imaging system, thereby achieving accurate length measurements. The actual object length corresponding to a specific length in the image is calculated based on the number of pixels using the following formula:

$$L_{real} = N_p \times l_p \div \beta \quad (1)$$

where L_{real} represents the calculated length, l_p represents the pixel size of the sensor, N_p represents the number of pixel size, β represents the magnification of the optical magnification lens (eyepiece×objective).

In the imaging process, the main sources of error are the CMOS sensor and the optical lens. In the imaging process of CMOS sensors, the conversion of light signals into electrical signals also introduces noise. Light reflected from external objects passes through the optical lens and arrives at the CMOS sensor. As the sensor captures the light signal, random fluctuations occur as the photons are collected by the photodiode, introducing photon shot noise and photon scatter noise00. In addition, sensor process errors result in dark current shot noise and dark current fixed pattern noise during sensor exposure. At the same time, reset noise, source follower noise and offset fixed pattern noise are introduced as the electrons are converted to voltage [19-21]. When the voltage signal is converted to a digital signal, quantization noise (quantization error of the analogue-to-digital conversion) is introduced. Dark current shot noise, dark current fixed pattern noise, reset noise, source follower noise, and offset fixed pattern noise can be represented as read noise, which follows a Gaussian distribution. In summary, the image noise in CMOS sensors can be expressed with the following formula:

$$\begin{aligned} H &= (F_1 I + M)F_2 \\ &= [F_1(I + M_1) + M_2 + M_3 + M_4]F_2 \end{aligned} \quad (2)$$

where H is the gray value of the output image, F_1 is the sensor analog gain, F_2 is the numerical gain, I is the total number of photoelectrons in a single image, M is the total noise, M_1 is the photon shot noise, M_2 is the read noise, M_3 is the row noise, M_4 is the quantization noise. The noise model of image process is shown in Fig. 2. When a CMOS sensor detects an external signal, it undergoes a process of converting that signal into an electronic form, then into a voltage signal, and finally into a digital representation. Throughout this conversion journey, different forms of noise are inadvertently introduced.

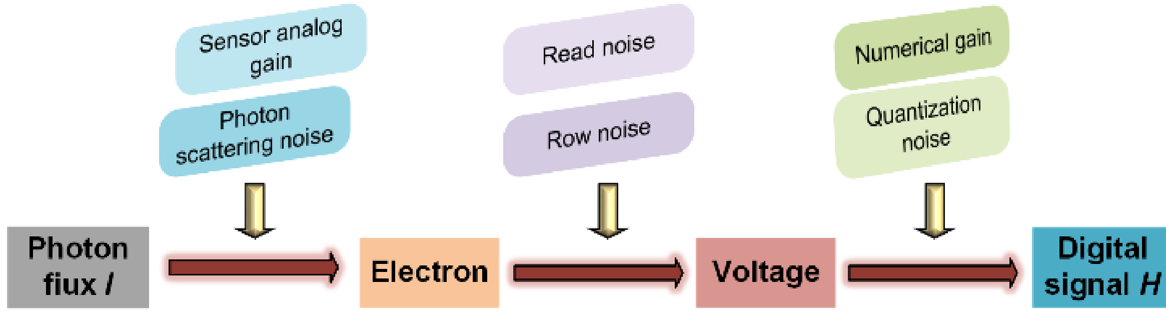

Fig. 2. Schematic diagram of imaging process (colour online)

The quantization nature of photons leads to uncertainty in the number of photons collected by the sensor, and this uncertainty follows a Poisson distribution.

$$(I + M_1) \propto P(I) \quad (3)$$

where P represents the adherence to a Poisson distribution.

The optical aberrations produced by a lens include spherical aberration, distortion, and chromatic aberration. Spherical aberration is an on-axis monochromatic aberration that results in a circular blur spot (a blurred image) of the target object. For a single lens, a concave lens produces positive spherical aberration (where the focal point of marginal rays is closer to the lens), while a convex lens produces negative spherical aberration (where the focal point of marginal rays is farther from the lens) [22,23]. The ideal image point A' of the object point A (on the optical axis) is intersected by the marginal rays emitted from A at point A_0', and the longitudinal spherical aberration $\delta L'$ is:

$$\delta L' = L' - l' \quad (4)$$

where L' is the distance from A_0' to the lens, and l' is the distance from A' to the lens. The spherical aberration of single lens is shown in Fig. 3.

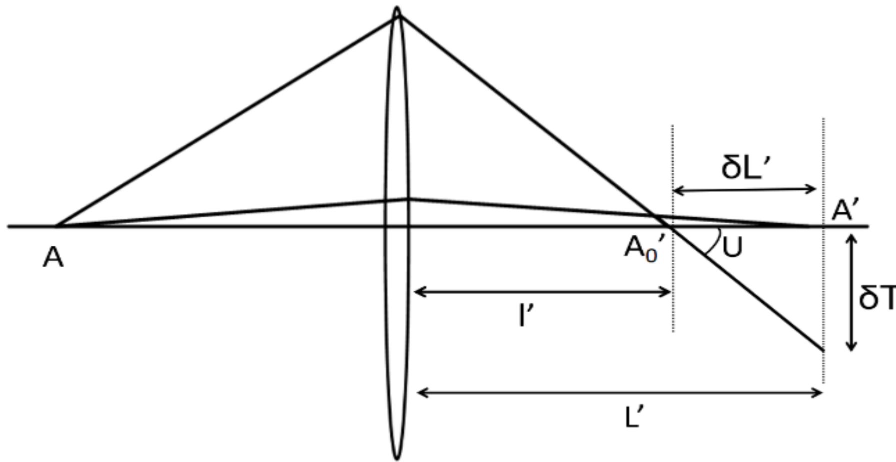

Fig. 3. Spherical aberration of single lens

The transverse spherical aberration δT is the radius of the blur spot caused by the spherical aberration in the axial direction:

$$\delta T = \delta L' \cdot tanU \quad (5)$$

where U represents the angle between the marginal ray after passing through the lens and the optical axis.

In real optical systems, the magnification varies at different points in the object and image planes, causing distortion in the object's image. This type of aberration is called distortion. Distortion can cause pincushion distortion and barrel distortion. Pincushion distortion (positive distortion) can cause a square object symmetrical to the optical axis to appear as a pincushion-shaped image, with the magnification increasing as the field of view increases. In contrast, barrel distortion (negative distortion) has a magnification that decreases as the field of view increases, causing a square object symmetrical to the optical axis

appears as a barrel-shaped image. The height at which the principal ray intersects the ideal image plane is y', and the height of the ideal image point is y_0'. The difference between them is the linear distortion:

$$\delta y' = y' - y_0' \tag{6}$$

Relative distortion is often referred to in terms of distortion, expressed as:

$$q = \frac{\delta y'}{y_0'} \times 100 \tag{7}$$

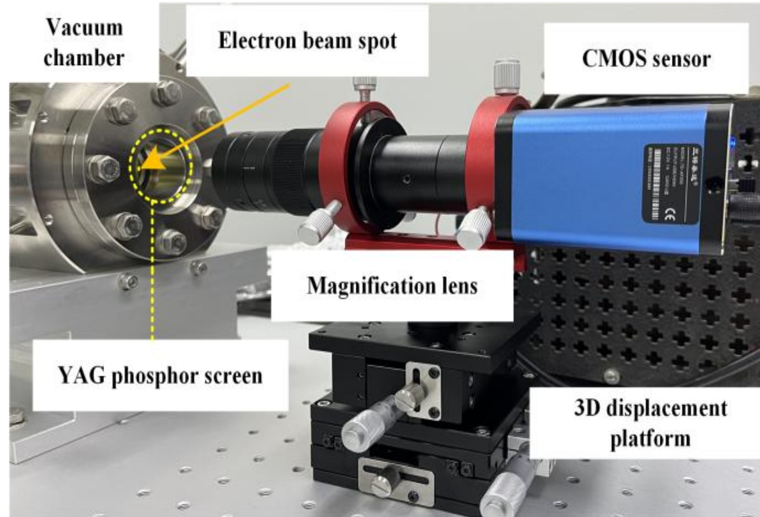

Fig. 4. Imaging measurement system (colour online)

The imaging measurement system device is shown in Fig. 4, the whole system is located on the right side of the vacuum chamber developed by ourselves, aligned with the YAG phosphor screen inside the observation window. The image of electron beam spot passes through magnification lens and then reaches the plane of CMOS sensor. At different magnifications, multiple photographs were taken of the same area on the steel ruler (with 20 photographs taken as mentioned in the text). The CMOS sensor is Sony IMX307 which has a 1/2.8-inch sensor size and a pixel size of 2.9×2.9μm, with an output resolution of 1920×1080. The magnification at the eyepiece end of the optical magnification lens is 0.5 and is not adjustable, while the magnification of the objective is adjustable (0.7-4.5). The total magnification is 0.35-2.25. Images of the same area on the steel ruler were taken at different magnifications, keeping the position of the ruler constant throughout the photographic process.

3. Results and discussion

Using the ImageView software, five groups of parallel lines were selected in the same region (1 mm width) of the ruler images for pixel length measurement. The pixel measurement process is shown in Fig. 5. The images at different magnifications were analyzed and parameters such as variance, standard deviation, and mean of the measurement data at different magnifications were calculated to evaluate the performance of the measurement system.

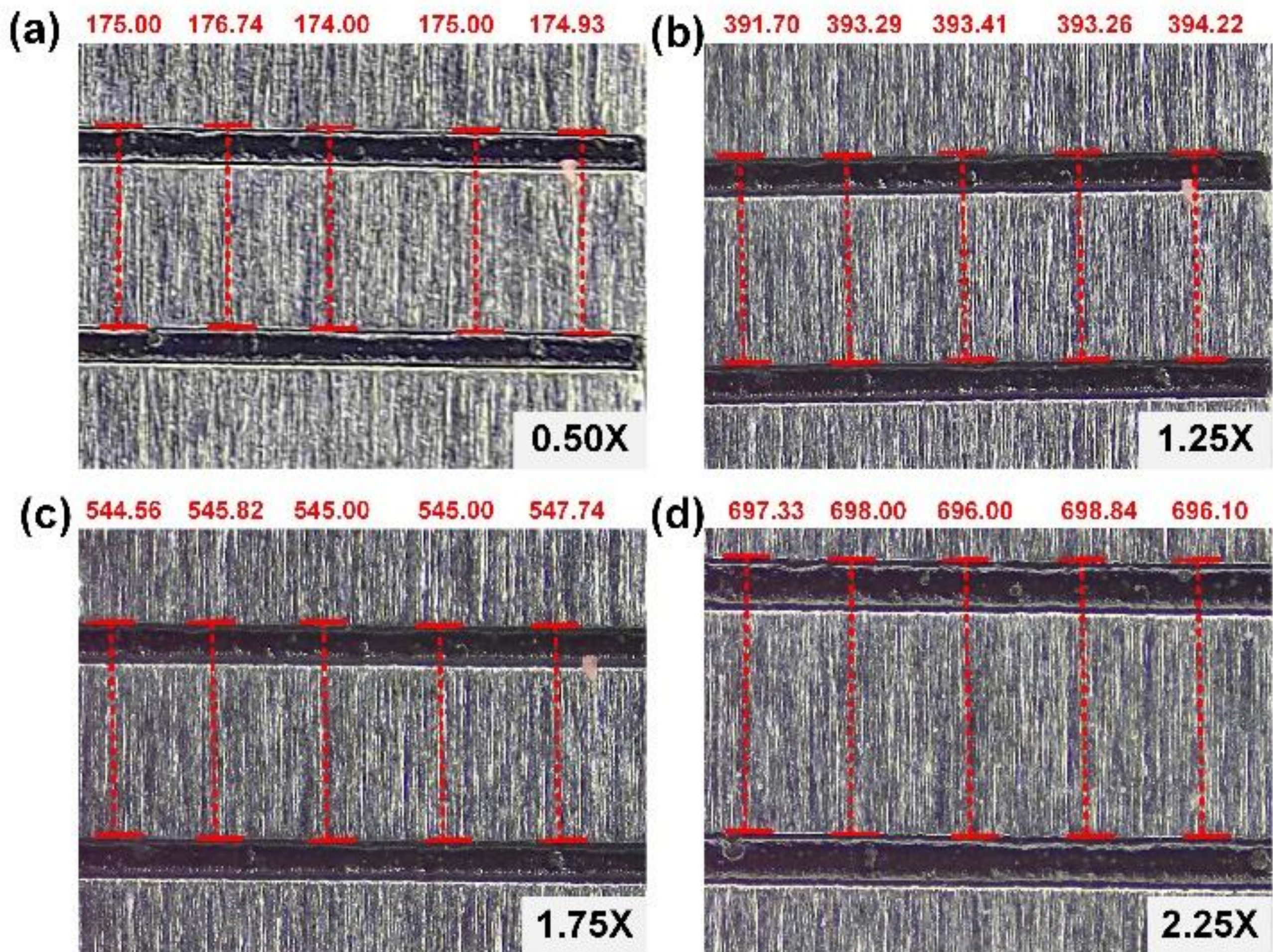

Fig. 5. Pixel measurements under different magnification levels (a)0.50x (b)1.25x (c)1.75x (d)2.25x (colour online)

In the experimental process, measurements and calculations were performed on the sample variance, sample standard deviation, and mean of these images with 9 different magnification states. The results are presented in Fig. 6 and Fig. 7. Due to environmental light noise during the image acquisition process and systematic errors associated with manual selection of parallel lines, the variance and standard deviation of the pixel calculation results exhibit certain fluctuations. At different magnifications, the pixel mean of the test images randomly varies within a range that is centered around the overall pixel mean.

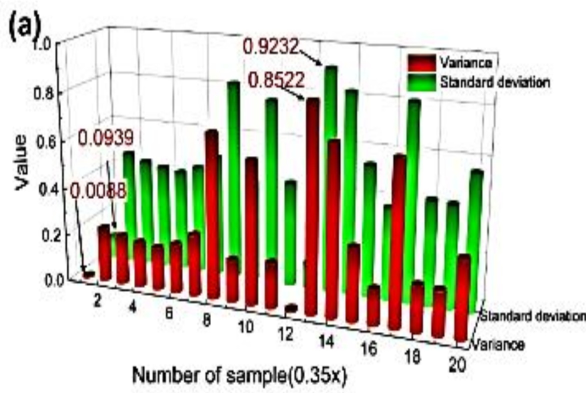
(a)
Value
Variance
Standard deviation
0.9232
0.8522
0.0939
0.0088
Number of sample(0.35x)

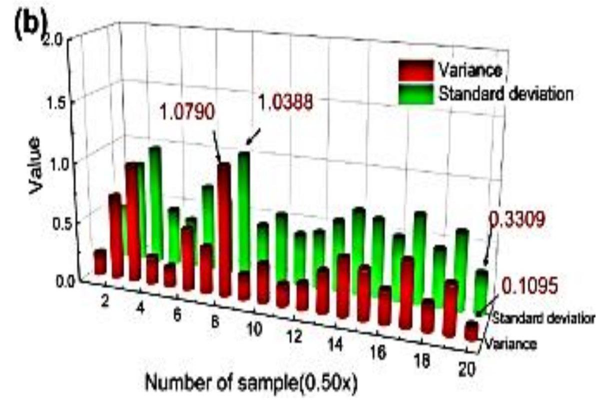
(b)
Value
Variance
Standard deviation
1.0790
1.0388
0.3309
0.1095
Number of sample(0.50x)

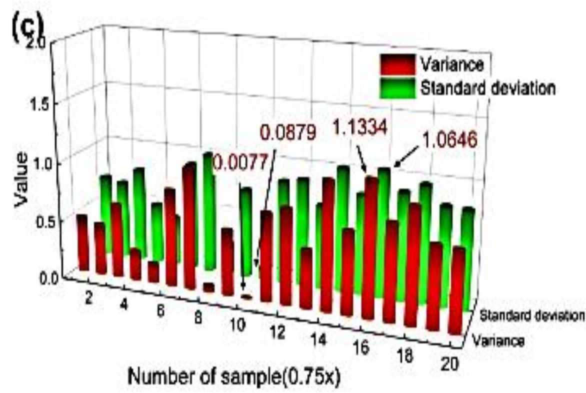
(c)
Value
Variance
Standard deviation
0.0879
1.1334
1.0646
0.0077
Number of sample(0.75x)

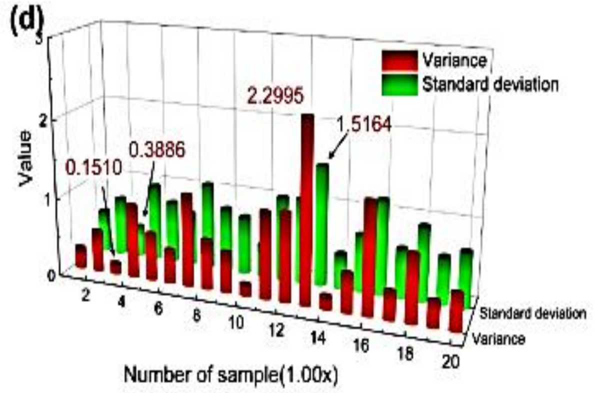
(d)
Value
Variance
Standard deviation
2.2995
1.5164
0.1510
0.3886
Number of sample(1.00x)

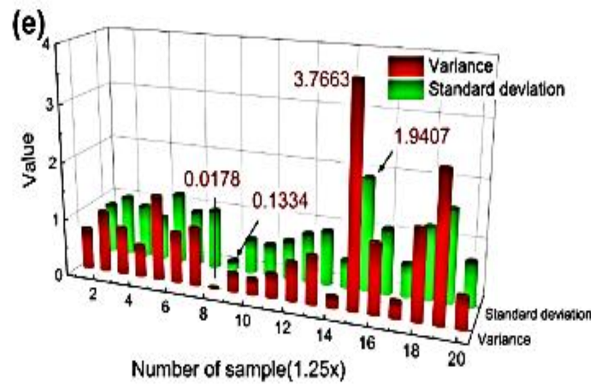
(e)
Value
Variance
Standard deviation
3.7663
1.9407
0.0178
0.1334
Number of sample(1.25x)

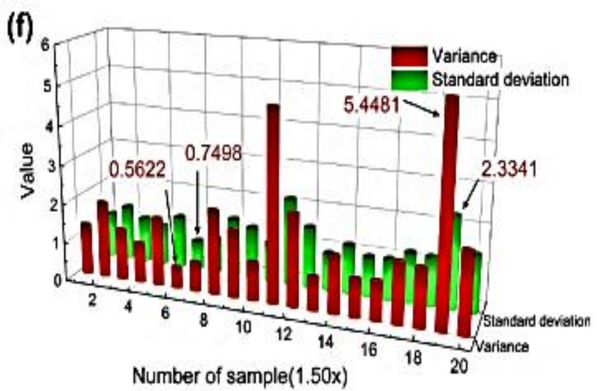
(f)
Value
Variance
Standard deviation
5.4481
2.3341
0.5622
0.7498
Number of sample(1.50x)

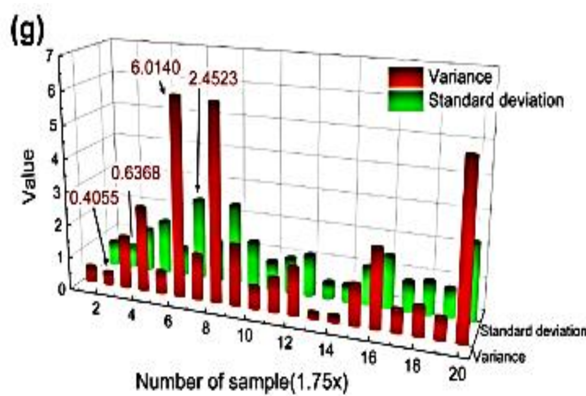
(g)
Value
Variance
Standard deviation
6.0140
2.4523
0.6368
0.4055
Number of sample(1.75x)

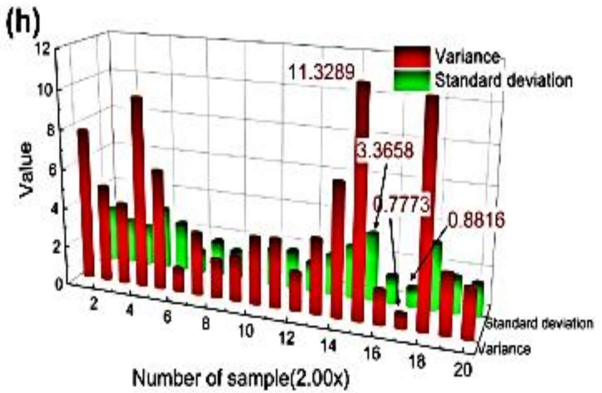
(h)
Value
Variance
Standard deviation
11.3289
3.3658
0.7773
0.8816
Number of sample(2.00x)

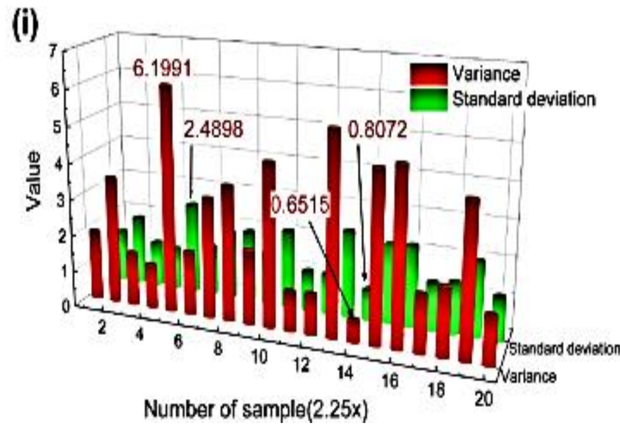

Fig. 6. Distribution of sample variance and standard deviation under different magnification levels (colour online)

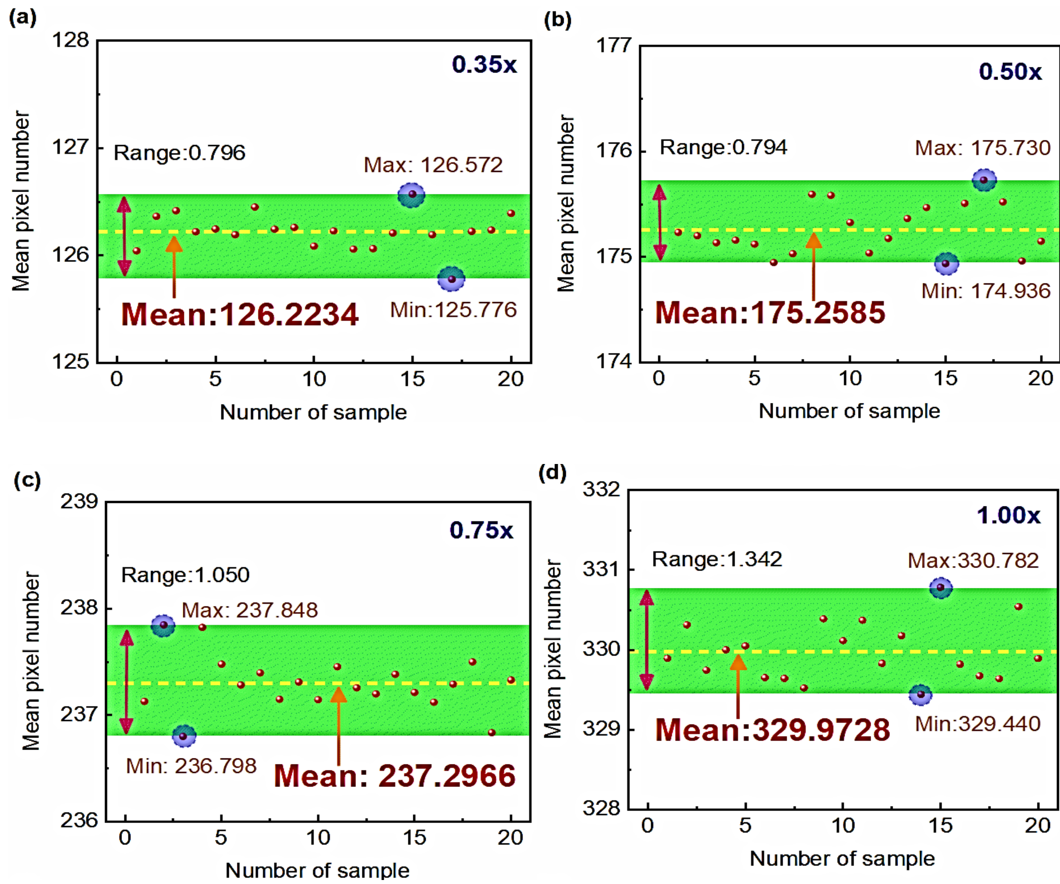

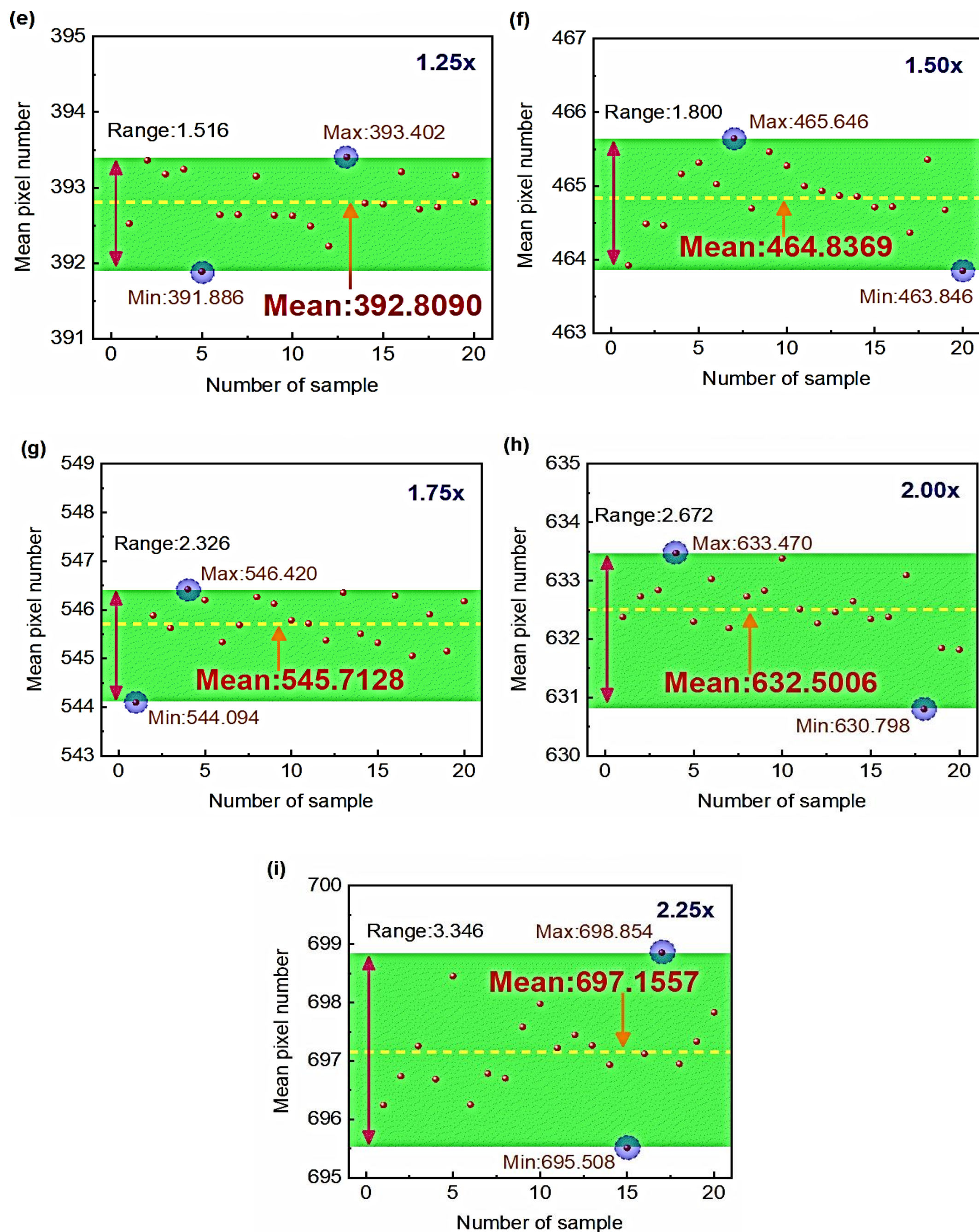

Fig. 7. Distribution of sample means under different magnification levels (colour online)

In order to eliminate errors due to the working fatigue of the CMOS sensor, a sampling analysis was performed on the pixel mean of samples 5, 10, 15, and 20 from each photo group under different magnification conditions. The results are shown in Fig. 8. The results indicate that the sampling results of different numbered samples are essentially the same, which does not affect the analysis results. The linear correlation fits of the four selected image groups are all 0.998, and the corresponding linear fit slopes range from 301.269 to 302.371. These slight variations in slope are due to random measurement error and are within acceptable limits.

The uncertainty in length measurement results primarily arises from two sources: the repeatability of sample measurements (Type A) and the coefficient of linear expansion of the sample (Type B). To calculate the standard

uncertainty μ_1 (using equation 8), we analyzed 20 photographs of samples taken at different magnifications (n=20). Additionally, μ_2 represents the uncertainty introduced by the coefficient of linear expansion (considering a temperature change ΔT of 4 ℃ and a measured length l_1 of 1 mm). The coefficient of linear expansion for stainless steel (α_1) is 17.2×10⁻⁶/℃. The resulting combined uncertainty μ is presented in the below Table 1. And μ_2 and μ are calculated according to equations 9 and 10.

$$\mu_1 = \sqrt{\frac{\Sigma(x_i - \bar{x})}{n-1}} \tag{8}$$

$$\mu_2 = \Delta T \times \alpha_1 \times l_1 \tag{9}$$

$$\mu = \sqrt{\mu_1^2 + \mu_2^2} \tag{10}$$

where x_i is the average pixel length of each sample (1mm), $\bar{x}$ is the average pixel length of all samples, and n is the number of samples (n=20).

Table 1. Uncertainty of the imaging system

Magnification	μ_1/μm	μ_2/μm	μ/μm
0.35	0.5015	0.1376	0.5200
0.50	0.6955		0.7090
0.75	0.7545		0.7669
1.00	1.0537		1.0626
1.25	1.1330		1.1413
1.50	1.3810		1.3878
1.75	1.6394		1.6452
2.00	1.7273		1.7328
2.25	2.2289		2.2331

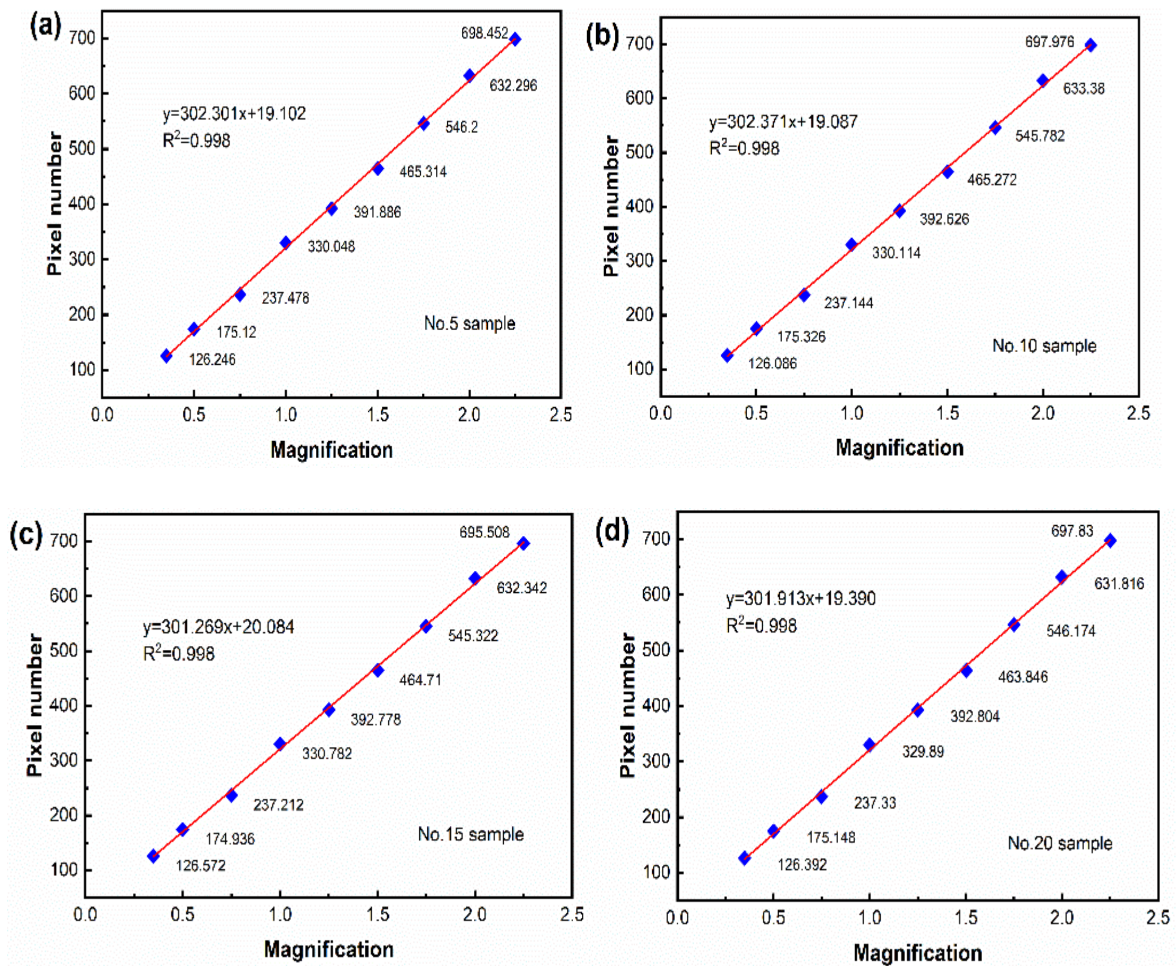

Fig. 8. Distribution of mean values for different sample numbers under various magnification levels (a) Sample 5 (b) Sample 10 (c) Sample 15 (d) Sample 20 (colour online)

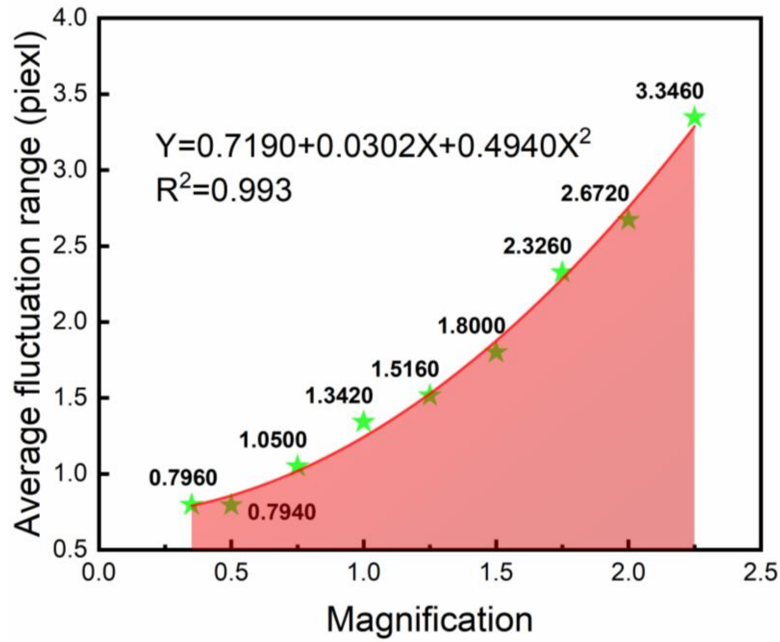

Fig. 9. Correction coefficients and corrected lengths under different magnification levels (colour online)

As shown in Fig.7, the fluctuation range of the sample means varies at different magnifications. As the magnification increases, the fluctuation range of sample means also gradually increases, showing a positive correlation. The calculation results of the fluctuation range of sample means are presented in Fig. 9.

The calculation and analysis data during the experimental process are presented in Table 2. Images collected at different magnifications were processed and analyzed. Given that the known target length is 1mm, and the systematic and random errors of the measurement process were taken into account, a correction coefficient was introduced during the calculation. The formula for calculating the corrected length, after introducing the correction coefficient, is as follows:

$$L_{real} = N_p \times B_p \times l_p \div \beta \tag{11}$$

where B_p is the correction coefficient, which represents correction of whole system error.

Table 2. Error calculation data of the imaging system

Magnification	Pixel number /mm	Calculated length	Error	Error rate	Corrected length	Corrected coefficient
0.35	126.2234	1045.8510 μm	45.8510	4.585%	1000.0427 μm	0.9562
0.50	175.2585	1016.4993 μm	16.4993	1.650%	1000.0261 μm	0.9838
0.75	237.2966	917.5469 μm	-82.4531	-8.245%	1000.0344 μm	1.0899
1.00	329.9728	956.9211 μm	-43.0789	-4.308%	999.9826 μm	1.0450
1.25	392.8090	911.3169 μm	-88.6831	-8.868%	999.9880 μm	1.0973
1.50	464.8369	898.6847 μm	-101.3153	-10.132%	999.9665 μm	1.1127
1.75	545.7128	904.3241 μm	-95.6759	-9.568%	1000.0016 μm	1.1058
2.00	632.5006	917.1259 μm	-82.8741	-8.287%	1000.0341 μm	1.0904
2.25	697.1557	898.5562 μm	-101.4438	-10.144%	1000.0032 μm	1.1129

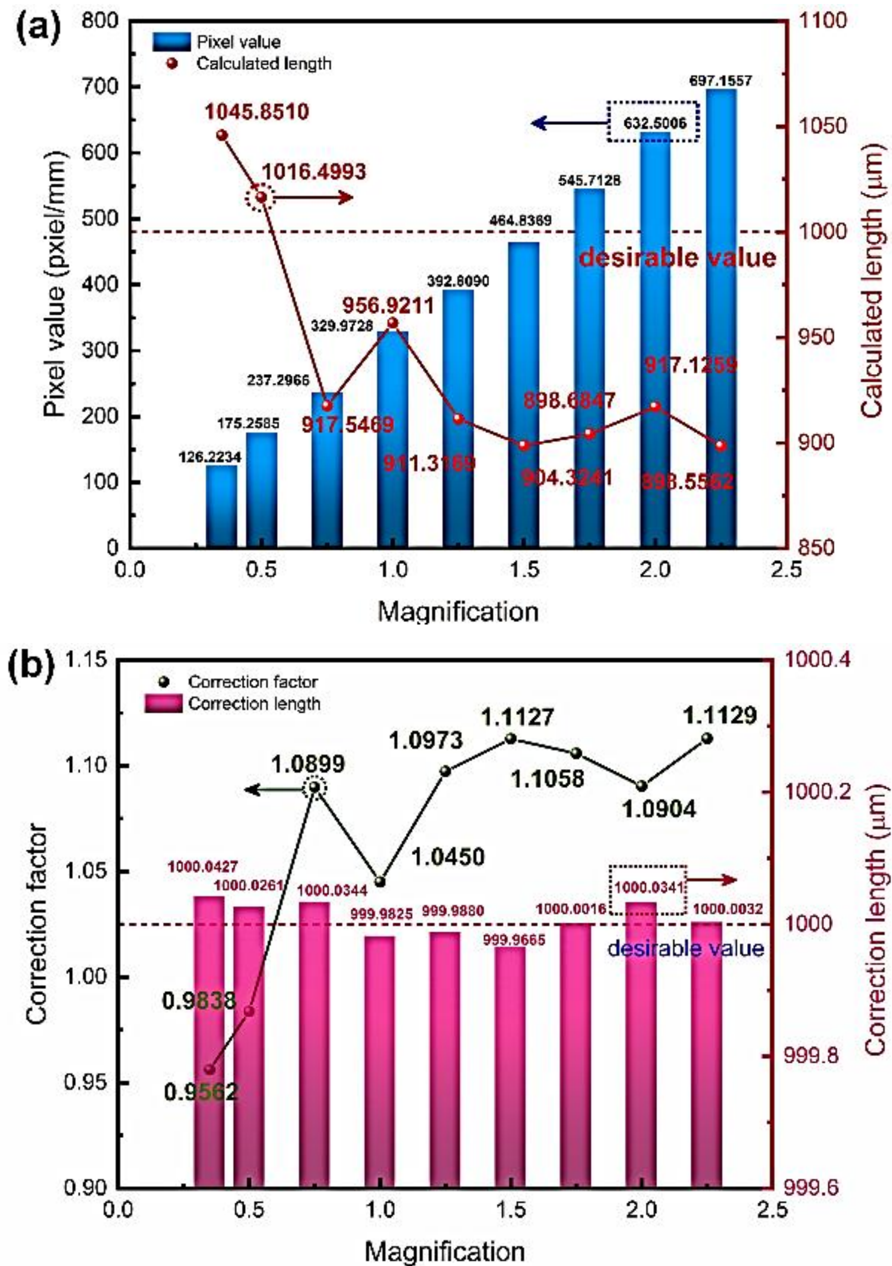

Fig. 10. Sample length measurement (a) Mean value and calculated length (b) Correction coefficient and corrected length (colour online)

During the experimental testing process, the main sources of error were aberrations from the magnification lens and systematic errors related to the testing method. In addition, environmental light noise partly contributed to variations in the experimental results. Given the known length of the target area, all measurement errors were combined into a single correction coefficient, which adjusts the calculated lengths at different magnifications to match the ideal length. The results of the correction coefficient calculations are illustrated in Fig.10. The values of the correction coefficient are less than 1 for magnifications of 0.35 and 0.50, while greater than 1 for all other magnifications. This suggests an overall trend for the correction coefficient to increase with the magnifications.

4. Conclusions

The theory and methods of optical imaging were investigated in this paper, and an optical imaging system

was constructed with optical magnification lenses and a CMOS sensor. Images of a steel ruler were taken at various magnifications, and a detailed error analysis of the image data was conducted to evaluate the system's correction coefficient curve, resulting in highly accurate distance measurements. The analysis of the experimental results revealed the error characteristics and the correction curve of the imaging system. After analyzing and correcting the image error, the length measurement error was reduced to within ±0.043 μm (by subtracting 1 millimeter from the corrected length). The non-contact measurement method has made a significant contribution to the accurate and rapid measurement of large-sized light spots, and it is expected that it will be further expanded and improved in future applications, thereby enhancing the potential for further research in this field.

Acknowledgments

This paper was funded by National Natural Science Foundation of China [grant number: 52105440] and Research Instrument and Equipment Development Project of Chinese Academy of Sciences [grant number: PTYQ2024BJ0004].

References

[1] S. He, H. Tang, K. Zhang, C. Chen, J. Wang, Z. Zhu, J. Gao, C. Cui, X. Chen, IEEE T. Ind. Electron. **68**(3), 2345 (2020).

[2] S. Zimmermann, T. Tiemerding, S. Fatikow, IEEE/ASME T. Mech. **20**(5), 2031 (2014).

[3] N. Marturi, B. Tamadazte, S. Dembele, S. Dembele, N. Piat, IEEE T. Autom. Sci. Eng. **15**(1), 45 (2016)

[4] M. J. Kim, H. J. Park. R. J. Jung, C. Y. Won, S. O. Ohk, H. T. Kim, N. K. Roh, K. H. Yi, Skin Res. Technol. **30**(4), e13667 (2024)

[5] M. A. Sutton, N. Li, D. C. Joy, A. P. Reynolds, X. Li, Exp. Mech. **47**, 775 (2007).

[6] T. Nishitani, Y. Arakawa, S. Noda, A. Koizumi, D. Sato, H. Shikano, H. Lijima, Y. Honda, H. Amano, J. Vac. Sci. Technol. B. **40**(6), 064203 (2022).

[7] F. Wu, Z. Hu, L. Duan, K. Zhong, B. Xu, W. Liu, J. Yao, Acta Metrologica Sinica **44**(02), 310 (2023).

[8] M. Rasmussen, O. Nagy, S. Skupin, A. Stathopulos, L. Berge, P. U. Jepsen, B. Zhou, Opt. Express **31**(6), 9287 (2023).

[9] A. Sliwak, M. Jelen, S. Patela, Opto-Electron. Rev. **30**, e140147(2022).

[10] F. Li, G. Zhong, H. Yu, K. An, R. Zhou, IEEE Trans. Instrum. Meas. **73**, 1 (2024).

[11] S. Handa, T. Kimura, H. Mimura, H. Yumoto, S. Matsuyama, Y. Sano, K. Tamasaku, Y. Nishino, M. Yabashi, T. Ishikawa, K. Yamauchi, Nucl. Instrum. Meth. A **616**(2-3), 246 (2010).

[12] E. Yanez, M. Cywiak, D. Cywiak, Appl. Optics **58**(31), 8495 (2019).

[13] K. Purvis, R. Cisek, D. Tokarz. J. Chem. Educ. **96**(9), 1977 (2019).

[14] Y. Tan, F. Lin, M. Ali, Z. Su, H. Wong, Opt. Laser Eng. **169**, 107696 (2023).

[15] J. Z. Jelic, M. Bukumira, A. Dencevski, A. Senkic, L. Zuzic, B. Radatovic, N. Vujicic, T. Pajic, M. D. Rabasovic, A. J. Krmpot, Microsc. Microanal. **30**(4), 671 (2024)

[16] B. S. Rawat, S. K. Sharma, B. Choksi, V. Prahlad, U. K. Baruah, AIP Adv. **12**(12), 125103 (2022).

[17] J. Chen, X. Liu, L. Du, B. Song, X. Sun, Acta Opt. Sin. **44**(12), 1228007 (2024).

[18] M. Yang, Y. Qian, Y. Yan, S. Wu, Laser Opto-Electron. P. **60**(02), 325 (2023).

[19] C. Zhang, S. Yao, J. Xu. J. Semicond. **32**(11), 115005 (2011).

[20] O. E. Setala, M. J. Prest, K. D. Stefanov, D. Jordan, M. R. Soman, V. Vahanissi, H. Savin, Small, **19**(47), 2304001 (2023).

[21] Y. Luo, L. Fu, N. Jia, T. Wang, R. Li, B. Zhang, IEEE Access **12**, 78714 (2024).

[22] F. Thomas. Opt. Eng. **61**(8), 085101 (2022).

[23] S. Sheng, L. Li, Z. Xin, L. Sun, Acta Opt. Sin. **41**(14), 1412001 (2021).

*Corresponding author: gregg1986@sina.com; yinbh@mail.iee.ac.cn